

# Measurement of Absolute Absorption Cross Sections for Nitrous Acid (HONO) in the Near-Infrared Region by the Continuous Wave Cavity Ring-Down Spectroscopy (cw-CRDS) Technique Coupled to Laser Photolysis

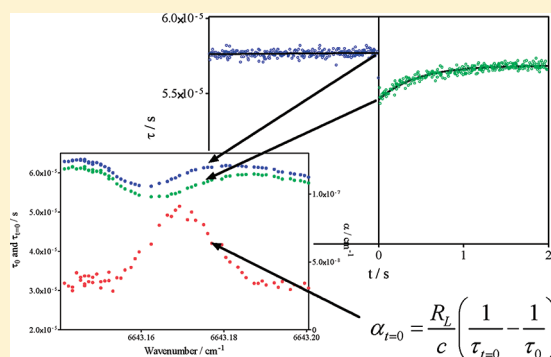
Chaithanya Jain,<sup>†</sup> Pranay Morajkar,<sup>†</sup> Coralie Schoemaeker,<sup>†</sup> Bela Viskolcz,<sup>‡</sup> and Christa Fittschen<sup>\*,†</sup>

<sup>†</sup>PhysicoChimie des Processus de Combustion et de l'Atmosphère, Université Lille Nord de France, PC2A CNRS Université Lille 1, UMR 8522, F-59650 Villeneuve d'Ascq, France

<sup>‡</sup>Department of Chemistry and Chemical Informatics, Faculty of Education, University of Szeged, Szeged, Boldogasszony sgt. 6, Hungary 6725

## Supporting Information

**ABSTRACT:** Absolute absorption cross sections for selected lines of the OH stretch overtone  $2\nu_1$  of the *cis*-isomer of nitrous acid HONO have been measured in the range  $6623.6\text{--}6645.6\text{ cm}^{-1}$  using the continuous wave cavity ring-down spectroscopy (cw-CRDS) technique. HONO has been generated by two different, complementary methods: in the first method, HONO has been produced by pulsed photolysis of  $\text{H}_2\text{O}_2/\text{NO}$  mixture at 248 nm, and in the second method HONO has been produced in a continuous manner by flowing humidified  $\text{N}_2$  over 5.2 M HCl and 0.5 M  $\text{NaNO}_2$  solutions. Laser photolysis synchronized with the cw-CRDS technique has been used to measure the absorption spectrum of HONO produced in the first method, and a simple cw-CRDS technique has been used in the second method. The first method, very time-consuming, allows for an absolute calibration of the absorption spectrum by comparison with the well-known  $\text{HO}_2$  absorption cross section, while the second method is much faster and leads to a better signal-to-noise ratio. The strongest line in this wavelength range has been found at  $6642.51\text{ cm}^{-1}$  with  $\sigma = (5.8 \pm 2.2) \times 10^{-21}\text{ cm}^2$ .



## INTRODUCTION

Nitrous acid (HONO) is an important chemical species in the atmosphere as well as in laboratory studies. In the atmosphere it is, especially in polluted areas, a major photochemical precursor for OH radicals in the early morning<sup>1</sup> but has also been detected in remote areas such as the south pole.<sup>2</sup> HONO can be produced in a simple gas phase reaction between OH radicals and NO, but heterogeneous reactions seem to be more important, and heterogeneous formation has been shown to occur on ice<sup>3</sup> but also on photocatalytic surfaces.<sup>4,5</sup> In laboratory studies, it has been identified as a heterogeneously formed, important OH radical precursor in atmospheric simulation chambers,<sup>6</sup> but also as a byproduct in the photolysis of  $\text{CH}_3\text{ONO}$ ,<sup>7</sup> another important OH-radical precursor for chamber studies. HONO can also be an interesting OH-precursor for laser photolysis studies, because it generates OH radicals after 351 nm excimer photolysis, thus avoiding possible unwanted complications arising at shorter, but more commonly used wavelengths.<sup>8,9</sup>

HONO is often detected and quantified by spectroscopic methods: UV-vis absorption using an open path differential optical absorption spectroscopy (DOAS) technique has been very successful for atmospheric measurements,<sup>10</sup> but Fourier

transform infrared (FTIR) spectroscopy has also been used, especially in laboratory studies.<sup>11</sup> While the qualitative absorption spectra of HONO have been studied by many authors in the UV-vis and IR range,<sup>12-16</sup> the major difficulty using spectroscopic detection methods is the uncertainty linked to the absolute absorption cross sections: HONO exists in an equilibrium with other components such as NO,  $\text{NO}_2$ ,  $\text{HNO}_3$ , and  $\text{H}_2\text{O}$  and is a rather unstable molecule, decomposing easily through heterogeneous reactions. Therefore, determining the absolute HONO concentration contained in an absorption cell is rather difficult. Febo et al.<sup>17</sup> have developed a method allowing the generation of stable HONO flows with very high purity, and this method has subsequently been used to determine absorption cross sections in the UV<sup>18</sup> and in the IR.<sup>19</sup>

Cavity enhanced absorption spectroscopy is getting more and more popular, especially in the near IR range, where cheap and reliable components such as distributed feedback (DFB) lasers and detectors are available. This makes this spectroscopic range

Received: March 31, 2011

Revised: August 29, 2011

Published: August 29, 2011

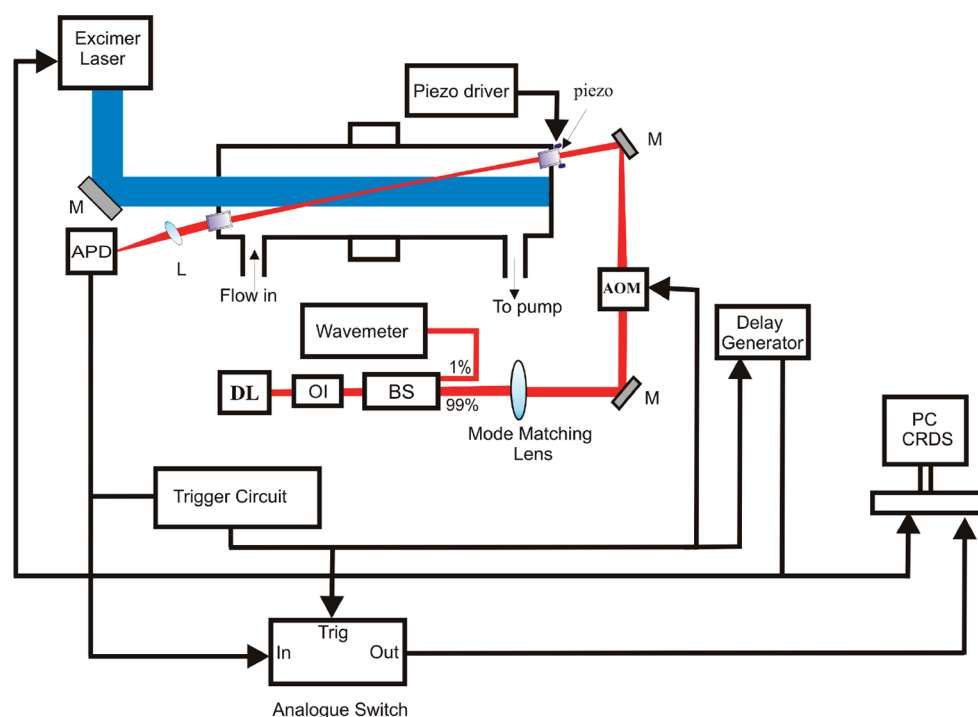


**Figure 1.** Schematic diagram of the experimental setup. APD = avalanche photo diode, DL = diode laser, OI = optical isolator, BS = beam splitter, AOM = acousto-optical modulator, M = mirror, and L = lens.

attractive, because now the rather small absorption cross sections expected for overtone transitions occurring in this wavelength range can be compensated for by the high sensitivity of the cavity enhanced methods.

HONO is known to exist in an equilibrium in two different forms, *trans*- and *cis*-HONO, in a ratio of approximately 2 to 1 in favor of the *trans* form.<sup>20</sup> The rovibrational parameters of both isomers, including the  $2\nu_1$  overtone of the OH stretch, have been published:<sup>14,15</sup> the band center of the  $2\nu_1$  overtone of the *cis*-isomer has been located at around  $6665\text{ cm}^{-1}$ , but no individual absorption lines have been assigned in this wavelength range. The  $2\nu_1$  overtone of the *cis*-isomer lies close to well-known and relatively intense  $2\nu_1$  overtone features of the HO<sub>2</sub> radical,<sup>21,22</sup> an important intermediate in the oxidation of volatile organic compounds (VOCs). The knowledge of absolute absorption cross sections for some HONO absorption lines in this wavelength range would allow for future, simultaneous measurements of HONO and HO<sub>2</sub> in laboratory studies.

Only one fairly indirect measurement of absorption cross sections for HONO is available in this range: Djehiche et al.<sup>7</sup> have detected HONO by continuous wave cavity ring-down spectroscopy (cw-CRDS) at  $6625.69\text{ cm}^{-1}$  as a reaction product during the photolysis of CH<sub>3</sub>ONO in a simulation chamber at a total pressure of 40 Torr of air. Through simultaneous measurements of CH<sub>2</sub>O and subsequent modeling they deduced the theoretical HONO concentration, postulating that it is formed in a reaction of OH radicals with the precursor CH<sub>3</sub>ONO. From this fairly indirect approach they have estimated the absorption cross section for *cis*-HONO to  $\sigma_{6625.69\text{ cm}^{-1}} = 4.2 \times 10^{-21}\text{ cm}^2$ , assuming that only 1/3 of the formed HONO is in *cis*-configuration.

In this work we present the measurement of the HONO spectrum in the range  $6623.6\text{--}6645.6\text{ cm}^{-1}$  using two different, complementary methods for generating HONO: pulsed and

continuous. The pulsed method has allowed determining absolute absorption cross sections, while the continuous method led to a better signal-to-noise ratio. The results presented in this work will allow quantitative determination of HONO in laboratory experiments.

## EXPERIMENTS

There are four main components to the experimental setup: the photolysis cell, the photolysis laser, the cw-CRDS system, and the laser-induced fluorescence (LIF) system. A detailed description of this setup has already been published,<sup>23,24</sup> and a schematic view of the experimental setup is given in Figure 1. The photolysis cell has three axes and is made of stainless steel, internally coated with Teflon. Photolysis is achieved along the longest axis with an excimer laser (Lambda Physik LPX 202i) operating at 248 nm. The beam entering the cell through a quartz window has a size of approximately  $1.5 \times 3.0\text{ cm}$ , with an energy of  $52\text{ mJ cm}^{-2}$ .

The LIF system has been used in the frame of this work for determining OH decays to accurately quantify the absolute H<sub>2</sub>O<sub>2</sub> concentration in the photolysis cell. The procedure has been described in detail in an earlier work<sup>24</sup> and will not be repeated here. The only change compared to the earlier work is that we now use instead of the photon counting devise a simple photomultiplier (Hamatsu R928) connected to a boxcar integrator (EG&G 4121B).

cw-CRDS, coupled to laser photolysis for some experiments, was used for the measurement of the HONO absorption spectrum. The principle of this technique has been published previously,<sup>23</sup> and recent improvements concerning the synchronization and acquisition can be found in a more recent work.<sup>24</sup> The mirrors used in this work (Los Gatos) had a reflectivity

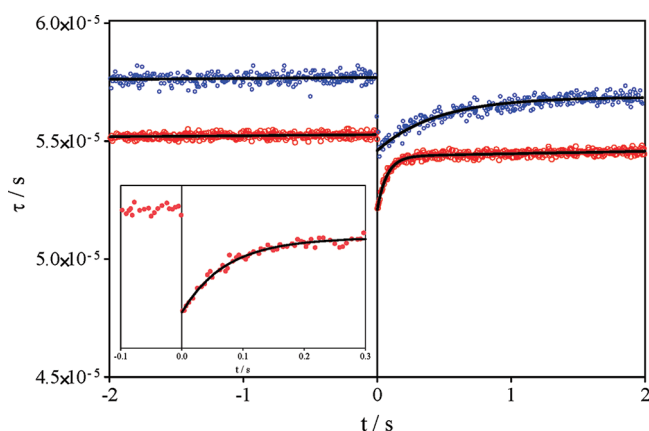


**Figure 2.** Typical time-resolved absorption signal for HONO formed from  $\text{H}_2\text{O}_2$  photolysis in the presence of NO. Red dots, 40 Torr helium; blue dots, 74 Torr  $\text{N}_2$ . The inset shows a zoom of the first 300 ms for the experiment in 40 Torr helium.

of  $R = 0.999954$ , leading to ring-down times in the empty cavity of around  $60 \mu\text{s}$ . Under our conditions ( $[\text{HONO}] = 3.1 \times 10^{13} \text{ cm}^{-3}$ , 37 cm absorption path) the strongest absorption lines led to a decrease in ring-down time of around  $5\text{--}10 \mu\text{s}$ .

The spectrum has been measured using two different methods of HONO generation, one based on a pulsed photolytic generation (a) and one based on a continuous, chemical synthesis (b).

(a) In the first method, HONO was produced in situ by the photolysis of hydrogen peroxide,  $\text{H}_2\text{O}_2$ , in presence of excess NO. Under these conditions, OH radicals initially formed from the  $\text{H}_2\text{O}_2$  photolysis are converted nearly quantitatively to HONO in a fast reaction sequence (see Results and Discussion). The ring-down events have to be measured relative to the photolysis pulse as explained in the previous publication.<sup>24</sup> A lab view program started the data acquisition and triggered simultaneously a delay generator which in turn triggered after 2 s the excimer laser. Ring-down events were recorded over a total period of 4 s, that is, 2 s before and 2 s after the photolysis pulse (see Figure 2). To renew the gas mixture between two laser pulses and to pump out most of the HONO produced during the previous laser pulse, photolysis was carried out at a repetition rate of maximal 0.08 Hz. To ensure that the data acquisition and the fitting of the individual ring-down events had been completed before the next photolysis pulse, the lab-view program was made to verify that data acquisition and fitting of the ring-down events is finished before starting the next data acquisition cycle. A minimum of 500 ring-down events have been acquired over the full 4 s measurement time (asking in average for 2–5 photolysis pulses) before the cw-CRDS laser was tuned by the Lab View program to the next wavenumber. The whole spectrum was measured with a resolution of  $0.005 \text{ cm}^{-1}$ ; that is, 4600 time-resolved traces as shown in Figure 2 have been recorded.

(b) In the second method, a stable concentration of HONO was produced in a continuous manner outside the cell by passing a calibrated flow of humidified  $\text{N}_2$  over 5.2 M HCl solution kept at  $12^\circ\text{C}$  followed by a 0.5 M solution of  $\text{NaNO}_2$ . The absorption spectrum was measured continuously; 25 ring-down events were averaged before the cw-CRDS diode laser was tuned to the next wavenumber. The whole spectrum was measured with a resolution of  $0.005 \text{ cm}^{-1}$ . The spectrum as shown in the Supporting Information has been measured in seven individual portions of

roughly  $3 \text{ cm}^{-1}$ ; the acquisition time of each portion was around 1 h. The method of HONO generation, described above, leads to a stable HONO concentration on a short time scale (1 h). However, the acquisition time of the whole spectrum was too long to assume a constant HONO concentration. Therefore, at the end of each individual portion, we have measured the absorption line at  $6643.17 \text{ cm}^{-1}$  and have normalized each portion of the spectrum with respect to this individual line. Thereafter, the HONO flow has been replaced by pure  $\text{N}_2$ , and the baseline for the individual portion was measured.

All data have been acquired using an acquisition card (National Instruments PC-6259) installed in a personal computer, and all programs were written in the Lab View software version 8.2.1. The experiments for the full spectrum were conducted at a total pressure of 40 Torr. For method (a)  $40 \text{ cm}^3 \text{ min}^{-1}$  standard temperature and pressure (STP) He was bubbled through a 50%  $\text{H}_2\text{O}_2$  solution (Sigma Aldrich), and  $1 \text{ cm}^3 \text{ min}^{-1}$  STP of NO (99%, Air Liquide) was added and mixed with the main flow of  $200 \text{ cm}^3 \text{ min}^{-1}$  STP He. A  $52 \text{ mJ cm}^{-2}$  photolysis energy leads to an initial OH concentration of  $3.3 \times 10^{13} \text{ cm}^{-3}$ , leading to a HONO concentration of  $3.1 \times 10^{13} \text{ cm}^{-3}$  (for details see next paragraph). For method (b)  $50 \text{ cm}^3 \text{ min}^{-1}$  STP  $\text{N}_2$  was flown over HCl (maintained at  $12^\circ\text{C}$  by a thermostat) and  $\text{NaNO}_2$  solution and mixed with a main flow of  $100 \text{ cm}^3 \text{ min}^{-1}$  STP He, leading to an average HONO concentration of  $1.7 \times 10^{13} \text{ cm}^{-3}$ . The most intense line has been measured also at different pressures (10, 40, and 73 Torr of  $\text{N}_2$  and He).

## RESULTS AND DISCUSSION

The full HONO absorption spectrum has been measured in 40 Torr He using two different complementary methods of HONO generation, a pulsed (a) and a continuous (b) manner.

(a) **Pulsed HONO Generation by Laser Photolysis.** Photolysis of  $\text{H}_2\text{O}_2$  at 248 nm leads to the formation of two OH radicals,<sup>25,26</sup> which reacts in the absence of other reaction partners in the following reaction sequence



In the beginning, OH radicals will predominantly react with  $\text{H}_2\text{O}_2$  to form  $\text{HO}_2$  radicals R2. As the reaction advances and  $\text{HO}_2$  radical concentration increases, reaction R3 becomes more or less important, depending on initial  $\text{H}_2\text{O}_2$  concentration and photolysis energy.<sup>27</sup> Finally at longer reaction times, the  $\text{HO}_2$  radicals recombine R4. The  $\text{H}_2\text{O}_2$  concentration used for the HONO generation has been measured regularly by cw-CRDS through its absorption line at  $6639.88 \text{ cm}^{-1}$  ( $\sigma = 2.23 \times 10^{-22} \text{ cm}^2$ , paper in preparation) and occasionally through OH decays (see Figure 3), obtained by LIF, and was  $[\text{H}_2\text{O}_2] = 2.9 \times 10^{15} \text{ cm}^{-3}$ , while the time-resolved  $\text{HO}_2$  profile has been measured at  $6638.20 \text{ cm}^{-1}$  ( $\sigma_{40\text{Torr}} = 2.93 \times 10^{-19} \text{ cm}^2$ ). A fit of these  $\text{HO}_2$ -profiles using the well-known rate constants for R2 – R4 leads to an initial OH concentration of  $[\text{OH}]_0 = 3.3 \times 10^{13} \text{ cm}^{-3}$ . The calculation of the OH concentration using the photolysis energy ( $52 \text{ mJ cm}^{-2}$ ) and  $\text{H}_2\text{O}_2$  absorption cross

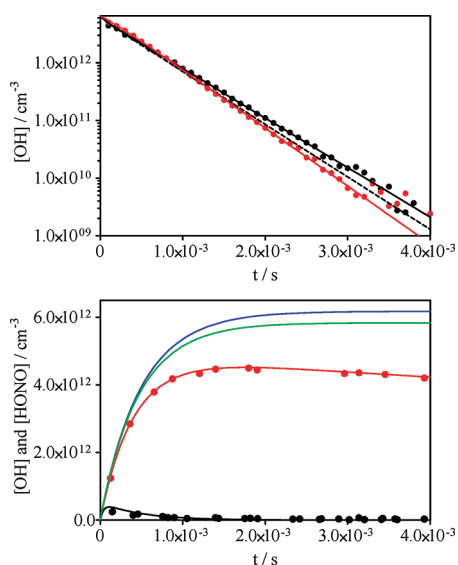


**Figure 3.** OH and HO<sub>2</sub> profiles for an experiment at 10 Torr N<sub>2</sub> with [H<sub>2</sub>O<sub>2</sub>] = 1.1 × 10<sup>15</sup> cm<sup>-3</sup> and [OH]<sub>0</sub> = 6.55 × 10<sup>12</sup> cm<sup>-3</sup>. Upper graph OH-decays: red dots, [NO] = 0; black dots, [NO] = 2.5 × 10<sup>15</sup> cm<sup>-3</sup>; full lines represent the simulation with rate constants as given in the text, dashed line the simulation with the additional impurity of [NO<sub>2</sub>] = 2.5 × 10<sup>13</sup> cm<sup>-3</sup>; lower graph experimental HO<sub>2</sub> profiles with simulations: blue line, simulated HONO profile without NO<sub>2</sub> impurity; green line, HONO profile in presence of NO<sub>2</sub> impurity.

section at 248 nm ( $\sigma_{\text{H}_2\text{O}_2,248\text{nm}} = 9.37 \times 10^{-20} \text{ cm}^2$ )<sup>28</sup> leads to [OH] = 3.52 × 10<sup>13</sup> cm<sup>-3</sup>, in very good agreement with the value obtained from cw-CRDS measurements.

The addition of NO to the reaction mixture will lead to a competition between R2 and



The reaction R5 is still in the falloff range at pressures of 40 Torr He with a low pressure rate constant<sup>29</sup> of  $k_{5,0} = 6.0 \times 10^{-31} \times [\text{He}] \text{ cm}^6 \text{ molecule}^{-2} \text{ s}^{-1}$ . However, HO<sub>2</sub> radicals formed through R2 even in the presence of NO in competition will rapidly be transformed back to OH through the fast reaction



The competing reaction channel



has been found to be very minor at room temperature at 200 Torr N<sub>2</sub>,<sup>30</sup> so it can safely be neglected under our conditions (40 Torr He). Another possible competing reaction for OH radicals is



and will gain some importance at longer reaction times with a rate constant<sup>31</sup> of  $k_7 = 7.0 \times 10^{-12} \text{ cm}^3 \text{ molecule}^{-1} \text{ s}^{-1}$ . The rate constants for R2 ( $k_2 = 1.7 \times 10^{-12} \text{ cm}^3 \text{ molecule}^{-1} \text{ s}^{-1}$ )<sup>32</sup> and R5 ( $k_5 = 6.0 \times 10^{-31} \text{ cm}^6 \text{ molecule}^{-2} \text{ s}^{-1} = 8.4 \times 10^{-13} \text{ cm}^3 \text{ molecule}^{-1} \text{ s}^{-1}$  at 40 Torr)<sup>29</sup> are comparable, leading at concentrations of H<sub>2</sub>O<sub>2</sub> (2.9 × 10<sup>15</sup> cm<sup>-3</sup>) and NO (5.1 × 10<sup>15</sup> cm<sup>-3</sup>) to similar pseudofirst-order rate constants of  $k_{2,5}^{\text{first}} \approx 5000 \text{ s}^{-1}$ . A simple simulation shows that under this condition 88.4% of initial OH radicals will be transformed into HONO within around 1 ms, that is, immediately on the time scale of

Figure 2: 7.2% of the initial OH radicals react through R3, and 4.4% react through R7; we can thus calculate [HONO] = 0.884 × [OH]<sub>0</sub> = 2.9 × 10<sup>13</sup> cm<sup>-3</sup>.

The systematic error introduced by uncertainties in the reaction mechanism is considered to be small: an error in the initial OH-radical concentration would of course have a direct, linear impact on the obtained HONO concentration; however, the impact on the HONO yield itself through a changed impact of R3 and R7 is negligible (see example further down). The initial OH concentration is mainly obtained from the absolute HO<sub>2</sub> concentrations, measured by cw-CRDS, while the H<sub>2</sub>O<sub>2</sub> concentration, measured through pseudo-first order OH decays and by absorption in the near IR, has only a minor impact on the extraction of the initial OH concentration. The absorption cross section of HO<sub>2</sub> is thought to be known to better than ±20%,<sup>21,22</sup> we therefore estimate the initial OH concentration to be known with the same accuracy. A possible systematic error source for the conversion of OH radical into HONO is impurity of NO<sub>2</sub>, arising from an oxidation of NO by trace amounts of O<sub>2</sub>: NO<sub>2</sub> reacts with both, OH and HO<sub>2</sub>, in addition reactions and would therefore decrease the HONO concentration. To illustrate the impact of such an impurity, typical experimental traces, together with model simulations, are shown for an experiment in 10 Torr of N<sub>2</sub>. The upper graph in Figure 3 shows experimental OH profiles together with simulations in the absence and presence of NO (2.5 × 10<sup>15</sup> cm<sup>-3</sup>): in the presence of NO, the OH decay is, under these conditions, slowed down due to the cycling of HO<sub>2</sub> radicals by R6a. Impurities of NO<sub>2</sub> however increase the decay rate of OH radicals drastically due to a reaction of NO<sub>2</sub> with both OH and HO<sub>2</sub> radicals: the dashed line in the upper graph represents an impurity of 2.5 × 10<sup>13</sup> cm<sup>-3</sup>, that is, 1% of the NO concentration. An impurity on this order of magnitude would be noticeable in our OH decays, and we therefore estimate an upper limit of the NO<sub>2</sub> impurity of 1% of the NO concentration. The lower graph in Figure 3 shows the corresponding HO<sub>2</sub> profiles: the red curve in the absence of NO is the basis for the calculation of the initial OH radical concentration, and it can be seen from the black dots that after NO addition HO<sub>2</sub> decreases rapidly to concentrations below our detection limit. The upper blue line shows the simulated HONO profile, which under these conditions corresponds to a HONO yield of [HONO] = 0.943 × [OH]<sub>0</sub> (a lower initial radical concentration compared to the conditions used for the complete spectrum leads to a decrease of the impact of R3). The green line shows the simulated HONO profile obtained in the presence of a 1% NO<sub>2</sub> impurity (2.5 × 10<sup>13</sup> cm<sup>-3</sup>): under these conditions, the HONO yield drops to 0.89, that is, a decrease of 5%. From the combined uncertainties ( $\sigma_{\text{HO}_2}$ , rate constants and NO<sub>2</sub> impurity), we estimate the uncertainty of the HONO concentration, and thus on the obtained absorption cross sections, to be ±30%.

From the time-resolved cw-CRDS signals (typical examples are shown in Figure 2), the absorbance  $\alpha_{t=0}$  and, now with knowledge of the photolytically generated HONO concentration, the absorption cross section  $\sigma$  can be extracted from:

$$\alpha_{t=0} = [\text{HONO}] \times \sigma = \frac{R_L}{c} \left( \frac{1}{\tau_{t=0}} - \frac{1}{\tau_0} \right) \quad (1)$$

where  $\alpha_{t=0}$  is the absorbance immediately after the photolysis pulse,  $R_L$  is the ratio between the cavity length  $L$ , that is, the distance between the two cavity mirrors, to the length  $L_A$  over which the absorber is present (in our case the overlap of

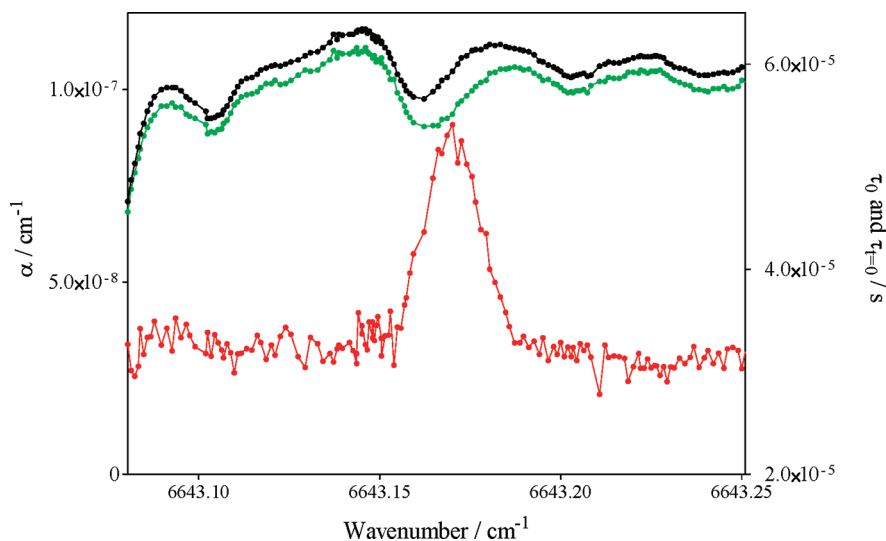


**Figure 4.** HONO spectrum obtained by laser photolysis: upper, black line is baseline ( $\tau_0$ ); middle, green line is  $\tau_{t=0}$  obtained through fits of individual, time-resolved HONO profiles to eq 2 (right Y-scale); and red line is absorbance  $\alpha$  obtained from eq 1 (left Y-scale).

photolysis beam and absorption path),  $c$  is the speed of light,  $\tau_0$  and  $\tau_{t=0}$  being the ring-down times before and immediately after the photolysis pulse, respectively. To extract  $\tau_{t=0}$  and  $\tau_0$ , the time-resolved signals as shown in Figure 2 have been analyzed for each wavelength by a data analysis program written in Lab View.  $\tau_0$  has been obtained as the intercept of the linear regression of all of the ring-down events that occurred during the 2 s before the photolysis pulse. For extracting  $\tau_{t=0}$ , all ring-down events occurred after the photolysis pulse have been fitted by a two phase association

$$\tau_t = \tau_{t=0} + a(1 - e^{-k_{\text{fast}}t}) + b(1 - e^{-k_{\text{slow}}t}) \quad (2)$$

HONO is a stable product; therefore the two empirical rate constants  $k_{\text{fast}}$  and  $k_{\text{slow}}$  can be interpreted by two different loss processes. The rapid decay with an average rate of  $k_{\text{fast},40\text{TorrHe}} \approx 12 \text{ s}^{-1}$  for the red dots (40 Torr Helium) can be linked to the diffusion of HONO out of the photolysis volume (to illustrate this process, the same experiment in 74 Torr of  $\text{N}_2$  is also shown in Figure 2 (blue dots): now, the rate is only  $k_{\text{fast},74\text{TorrN}_2} \approx 2 \text{ s}^{-1}$ ). This process is completed after roughly 200 ms (more than 1 s for 74 Torr  $\text{N}_2$ ); that is, after this delay the HONO, generated initially in the volume limited by the size of the photolysis beam, has diffused into the entire volume. The following slow loss  $k_{\text{slow}}$  with an average rate of  $k_{\text{slow}} \approx 0.16 \text{ s}^{-1}$  can possibly be approximated as the loss of HONO through processes such as the renewal of the gas mixture by pumping and heterogeneous losses on the reactor wall. To evaluate if this assumption is reasonable, one can carry out a simple estimation: the photolysis cell has an inner diameter of 6 cm leading to a surface of  $28.3 \text{ cm}^2$ , while the photolysis beam has a surface of  $4.5 \text{ cm}^2$ , that is, a ratio of 6.2 between photolyzed over total volume (for simplicity the side arms of the reaction cell have not been taken into account, which would increase this ratio). Taking a typical time-resolved signal such as shown in Figure 2, one can calculate the ratio of the absorbencies  $\alpha$ : taking into account that  $R_L$  (see eq 1) evolves from 2.22 just after the laser pulse (0.82/0.37) to 1.05 (0.82/0.78) at long reaction times, one finds a ratio of  $\alpha_{t=0}$  over  $\alpha_{t=200\text{ms}}$  of 7.2, in good agreement with the above calculated volume ratio.

We therefore are confident that the time-resolved evolution of the absorbance is due to diffusion phenomena only. One can notice that the renewal of the gas mixture is probably not totally completed just before the next photolysis pulse; that is, some HONO is still left in the photolysis cell (the baseline is not completely flat). This however has no influence on the calibration of the absorption measurement, because the laser photolysis technique accounts only for HONO that is formed from the actual photolysis pulse, all possible residual HONO will also contribute with the same intensity to the baseline. The same is true for any absorption due to other species present in the photolysis cell such as  $\text{H}_2\text{O}$ : these absorptions will not be visible, because it affects  $\tau_0$  and  $\tau_{t=0}$  in the same way (see Figure 7).

To illustrate the measurement principle, a small portion of the obtained spectrum (although not typical for the whole spectrum, because measured with a higher resolution of  $0.001 \text{ cm}^{-1}$ ) is presented in Figure 4: each set of dots (black, green, and red) at one given wavelength is the result of one time-resolved HONO signal as shown in Figure 2. The upper black line is the baseline, as obtained from ring down events acquired just before the photolysis pulse. The middle green dots have been obtained as  $\tau_{t=0}$  from fits of the individual, time-resolved HONO profiles to eq 2. The lower red line represents the absorbance  $\alpha$  as calculated from eq 1. In this manner the spectrum accessible with our DFB laser ( $6623.6\text{--}6645.6 \text{ cm}^{-1}$ ) has been measured with a resolution of  $0.005 \text{ cm}^{-1}$  and is presented in Figure 5. The repetition rate of the experiment was very low (0.08 Hz maximal); therefore the total measurement time for the spectrum shown in Figure 5 spread over 2 weeks. The generated HONO concentration depends directly on the  $\text{H}_2\text{O}_2$  concentration and on the photolysis energy. To ensure that the HONO concentration was constant over the whole measurement period, the  $\text{H}_2\text{O}_2$  concentration has regularly been checked by measuring its absorption line at  $6639.88 \text{ cm}^{-1}$ . The photolysis energy has also regularly been checked by a calibrated power meter. Occasionally,  $\text{HO}_2$  concentration–time profiles have been recorded in the absence of NO, verifying simultaneously the  $\text{H}_2\text{O}_2$  concentration and the photolysis energy.

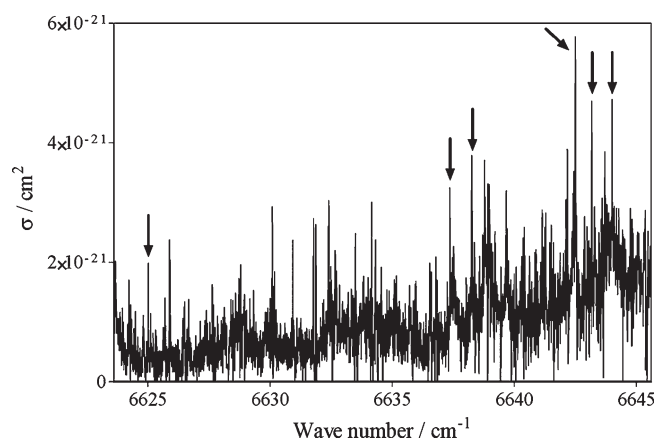


**Figure 5.** Full spectrum of HONO accessible with the DFB diode, obtained by pulsed HONO generation and calibrated to the six individual absorption lines indicated by an arrow.

It has been mentioned that the spectrum shown in Figure 5 has been measured for practical reasons at a low spectral resolution with a poor signal-to-noise ratio. However, this spectrum has been used to choose six of the most intense absorption lines to be remeasured very carefully with high spectral resolution to obtain a significant calibration. Six absorption lines, indicated by an arrow in Figure 5, have therefore been measured using a higher resolution ( $0.001 \text{ cm}^{-1}$ , the same as shown in Figure 4) and taking special care on the verification of the absolute HONO concentration: before starting the acquisition of each line, the  $\text{HO}_2$  and  $\text{OH}$  concentration–time profiles as well as the  $\text{H}_2\text{O}_2$  absorption around  $6639.88 \text{ cm}^{-1}$  have been measured in the absence of  $\text{NO}$ . The six individual lines have been submitted as Supporting Information, and the peak absorption cross sections of these lines in 40 Torr helium are listed in Table 1. It can be seen from Figure 4 (and from the figures in the Supporting Information) that a broad absorption underlies the individual absorption lines: this background absorption is unequivocally HONO, because it is generated by the photolysis pulse and is probably due to an unresolved, dense spectrum. Sometimes it is not possible to record a baseline in the absence of HONO; therefore we have added in Table 1 the percentage of the peak absorption cross section that is due to this background absorption. Please keep in mind that HONO is in equilibrium between its *cis*- and *trans*-isomer; that is, only around 1/3 of the photolytically generated HONO is present in form of the *cis*-isomer. This fact has not been taken into account in the calculation of the absorption cross sections, because the result of this work should be seen as a tool enabling the simple quantification of HONO in laboratory experiments. Under this point of view it seems idle to take into account that the *cis*–*trans* equilibrium and absorption cross sections given in this work can therefore be directly used to obtain total HONO concentrations and not only the concentration of the *cis*-population.

**(b). Continuous HONO Generation from  $\text{HCl}$  and  $\text{NaNO}_2$ .** It has been explained that the spectrum obtained by generating HONO in a pulsed manner could, for practical reasons, be obtained with a poor signal-to-noise ratio only. The pulsed method has other advantages, noticeably that (a) the absolute HONO concentration can be known from a calibration relative to  $\text{HO}_2$  profiles and that (b) other stable species present in the cell such as  $\text{H}_2\text{O}$  or products formed in an equilibrium with

**Table 1.** Line Strengths of Some Selected HONO Absorption Lines in the Near-Infrared Region<sup>a</sup>

wavenumber ( $\text{cm}^{-1}$ )	absorption cross-section ( $10^{-21} \text{ cm}^2$ )	background absorption (%)
6625.01	$1.6 \pm 1.0$	26
6637.36	$3.5 \pm 1.6$	38
6638.26	$3.8 \pm 1.6$	30
6642.51	$5.8 \pm 2.2$	37
6643.17	$4.2 \pm 1.7$	33
6644.00	$4.8 \pm 1.9$	52

<sup>a</sup> Errors have been estimated from the signal-to-noise ratio ( $\Delta\alpha = 1.5 \times 10^{-8} \text{ cm}^{-1}$ ) plus 30% for other errors such as drift in  $\text{H}_2\text{O}_2$  concentration, photolysis energy, and uncertainties in the retrieval of the HONO concentration. In the third column is added the percentage of this absorption cross section that is due to the congested background absorption.

HONO or from heterogeneous reactions at longer reaction times will not be detected: all absorption features appearing directly after the photolysis pulse are inherent to HONO. To obtain a spectrum with better signal-to-noise ratio, we have therefore remeasured the whole spectrum using a continuous source of HONO: humidified  $\text{N}_2$  was flown first over a 5.2 M  $\text{HCl}$  solution (kept at  $12^\circ\text{C}$ ) and then over a 0.5 M  $\text{NaNO}_2$  solution. First tests using the method developed by Febo et al.<sup>17</sup> did not lead to any signal, probably due to very low concentrations. We then tried a variant published by Barney et al.<sup>19</sup>, in which humidified  $\text{N}_2$  is flown over 5.2 M  $\text{HCl}$  (kept at  $0.0^\circ\text{C}$ ) and solid  $\text{NaNO}_2$ . However, the HONO concentration that could be generated by this method was still too low to obtain a spectrum with a satisfying signal-to-noise ratio. Therefore, a slight modification using  $\text{NaNO}_2$  in solution has been employed: this way, much higher concentrations of HONO could be obtained. A drawback of this modification is (a) the high water concentration in the reactor ( $\text{H}_2\text{O}$  has strong absorption lines in this wavelength region) and (b) the instability of the HONO concentration on the longer time scale: a slow increase in the HONO concentration on the hour-time scale was observed, possibly due to an increase in  $\text{NaNO}_2$  concentration following the slow evaporation of water. This change in HONO concentration was too fast to allow measuring the whole spectrum considering identical HONO concentrations. Therefore the spectrum has been measured in seven individual portions, and each portion has been calibrated to a reference: one of the HONO lines ( $6643.17 \text{ cm}^{-1}$ ) has been chosen as reference line and has been regularly measured before and after the acquisition of each portion of the spectrum; the absorbance of the entire portion was calibrated subsequently to the intensity of this line.

Once the whole spectrum has been measured and all individual portions have been calibrated to the reference line, the absorbance  $\alpha$  of the six HONO lines shown as Supporting Information were plotted against the absolute absorption coefficients  $\sigma$  of the same lines obtained by the pulsed method and tabulated in Table 1. This should present a linear relationship if the reference line calibration for the continuous spectrum is valid: as can be seen in Figure 6, this seems to be the case. The slope of a linear regression of this plot represents the HONO concentration generated by the continuous method:  $(1.58 \pm 0.2) \times 10^{13} \text{ cm}^{-3}$ .

A comparison of the spectra, obtained with both methods, is shown for a small portion in Figure 7; the entire spectrum has

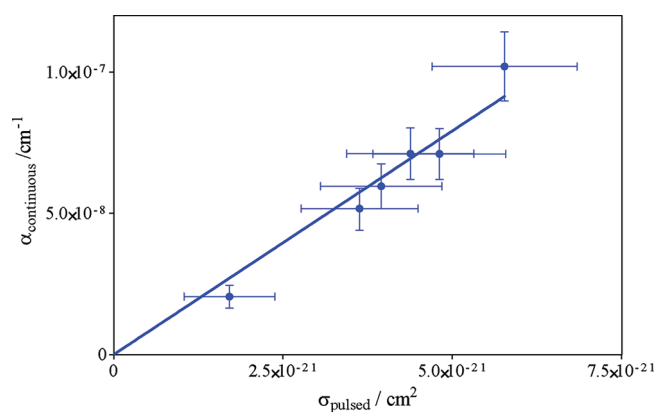


**Figure 6.** Plot of absorbance  $\alpha$  obtained by continuous HONO production against the absorption cross sections  $\sigma$  obtained by pulsed HONO generation for the six lines shown as Supporting Information.

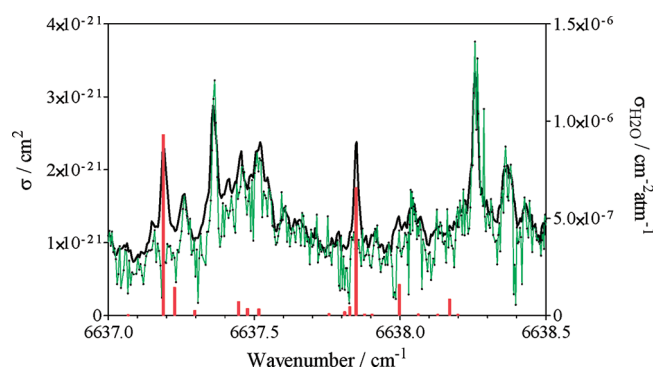


**Figure 7.** Small portion of HONO spectrum, obtained by both methods: the green line shows the spectrum obtained by laser photolysis method; the black line shows the spectrum obtained by continuous HONO production, and red spikes show the  $\text{H}_2\text{O}$  spectrum, as obtained by Macko et al.

been submitted as Supporting Information to this publication. The green line represents the spectrum obtained using the pulsed method, and the black line represents the spectrum obtained by the continuous method. For comparison, the position of  $\text{H}_2\text{O}$  absorption lines as published by Macko et al.<sup>33</sup> have been added to the graph (red spikes). It can be seen that the  $\text{H}_2\text{O}$  lines are clearly visible in the continuous HONO spectrum but do not appear in the pulsed HONO spectrum. The HONO absorption features on the other hand (for example, 6638.26 or 6639.36  $\text{cm}^{-1}$ ) are clearly visible in both spectra, continuous and pulsed. There is, however, a limitation even to the pulsed method: very strong  $\text{H}_2\text{O}$ -absorption lines (for example, 6626.5  $\text{cm}^{-1}$ , see Supporting Information) can decrease the intensity of the ring-down events below the trigger threshold and preventing measuring HONO absorption features.

The result of this work can be compared to the only published absorption cross section, deduced by Djehiche et al.<sup>7</sup> for the line at 6625.69  $\text{cm}^{-1}$ :  $\sigma = 4.2 \times 10^{-21} \text{ cm}^2$ . From looking at the whole spectrum, published as Supporting Information, it can be seen that this is a rather small line with an absorption cross section of  $\sigma = 3.2 \times 10^{-21} \text{ cm}^2$  (Djehiche et al.<sup>7</sup> have taken into account the cis–trans equilibrium, while in this work it has not been taken into account; hence  $\sigma$  from the Supporting Information has been multiplied by 3 for comparison). Djehiche et al.

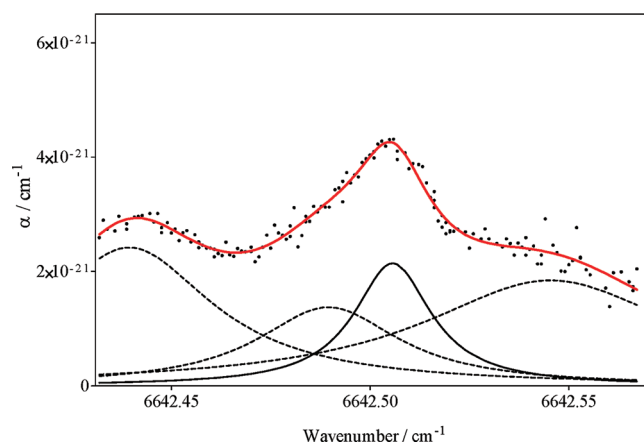
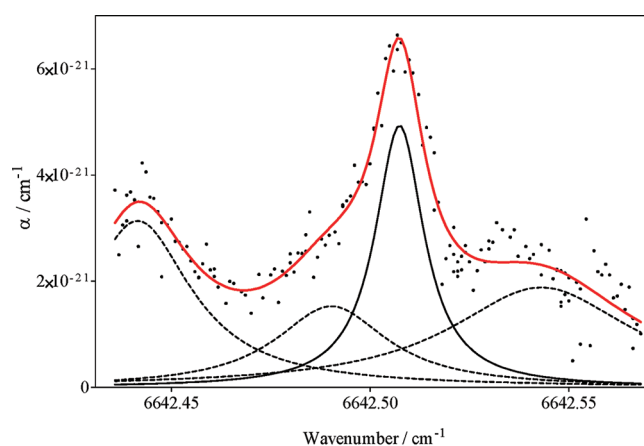


**Figure 8.** HONO absorption line at 6642.51  $\text{cm}^{-1}$ : upper graph at 10 Torr  $\text{N}_2$ , lower graph at 74 Torr  $\text{N}_2$ . The black lines represent the individual absorption lines identified by the Fityk program through a fit of the experimental data (black dots) to a Voigt profile.

measured in 40 Torr  $\text{N}_2/\text{O}_2$ , while the spectrum in this work has been obtained in 40 Torr He; therefore, the value of Djehiche et al. would be expected to be slightly smaller than the value obtained in this work due to pressure broadening (see next paragraph). However, the 30% higher absorption cross section from Djehiche et al. can still be considered in good agreement, looking at the very indirect method they have used to extract the absorption cross section.

**(c). Pressure Broadening of HONO Absorption Lines.** The goal of this work is to provide a tool for measuring absolute HONO concentrations in laboratory experiments under reduced pressures. For this reason, we have investigated the pressure broadening of the most intense line at 6642.51  $\text{cm}^{-1}$  in the pressure range 10–74 Torr with He and  $\text{N}_2$  as bath gas. In Figure 8 are shown the two lines obtained at 10 Torr  $\text{N}_2$  (upper graph) and at 74 Torr  $\text{N}_2$  (lower graph). It is apparent (and has already been discussed) that the background absorption is a convolution of nonresolved absorption lines, leading to broad background absorption. In Figure 8 we have illustrated this by adding the result of a least-squares fit of the experimental data to individual, Voigt-shaped absorption lines, obtained by the free software fitting program Fityk (Version 0.9.8).<sup>34</sup> From this figure it is obvious that it will not be useful to extract line strengths and pressure broadening coefficients for individual lines to propose a reliable tool to extrapolate absorption cross sections under various experimental conditions. Instead, we present the absorption cross

Table 2. Pressure-Dependent Absorption Cross Sections at the Center of the Strongest Line at 6642.51 cm<sup>-1a</sup>

pressure (Torr)	He		N <sub>2</sub>	
	$\sigma_{6642.51\text{cm}^{-1}}$ (10 <sup>-21</sup> cm <sup>2</sup> )	$\sigma_{6642.46\text{cm}^{-1}}$ (10 <sup>-21</sup> cm <sup>2</sup> )	$\sigma_{6642.51\text{cm}^{-1}}$ (10 <sup>-21</sup> cm <sup>2</sup> )	$\sigma_{6642.46\text{cm}^{-1}}$ (10 <sup>-21</sup> cm <sup>2</sup> )
10	7.0 ± 2.6	1.8 ± 1.0	6.6 ± 2.5	1.8 ± 1.0
40	5.8 ± 2.2	2.1 ± 1.1	5.1 ± 2.0	2.3 ± 1.2
74	4.6 ± 1.8	2.3 ± 1.2	4.3 ± 1.8	2.4 ± 1.2

<sup>a</sup>For practical purposes, the absorption cross section at 6642.46 cm<sup>-1</sup> is also given (see text).

sections in the center of the strongest absorption line in Table 2 for the three individual pressures and for both bath gases, He and N<sub>2</sub>. It is not always possible to measure the baseline in the absence of HONO, for example, in atmospheric simulation chambers. For this reason, we have also added the pressure-dependent minimum absorption cross section at 6642.46 cm<sup>-1</sup>.

## CONCLUSION

The near-IR spectrum of a portion of the 2ν<sub>1</sub> absorption band of the cis-isomer of HONO has been measured at a total pressure of 40 Torr helium in the range 6623.6–6645.6 cm<sup>-1</sup>, using two different methods for generating HONO. Absolute absorption cross sections for selected nitrous acid lines have been determined through calibration of the generated HONO concentration against the well-known HO<sub>2</sub> absorption cross section. The strongest line in this wavelength range has been found at 6642.50 cm<sup>-1</sup> with  $\sigma = (5.8 \pm 2.2) \times 10^{-21}$  cm<sup>2</sup>. Using current cw-CRDS setups, HONO concentrations of as low as 1 × 10<sup>12</sup> cm<sup>-3</sup> (corresponding to  $\alpha = 5 \times 10^{-9}$  cm<sup>-1</sup>) can easily be quantified at 40 Torr He. Pressure broadening up to 74 Torr has been measured of the most intense line for He and N<sub>2</sub> as bath gas. The results show that absorption spectroscopy in the near-IR range is not suitable for atmospheric measurements due to a too small absorption cross section combined with strong pressure broadening. However, it can provide an interesting tool for laboratory studies.

## ASSOCIATED CONTENT

**S Supporting Information.** Six individual lines measured at high resolution as well as the full spectrum as obtained with both methods. This material is available free of charge via the Internet at <http://pubs.acs.org>.

## AUTHOR INFORMATION

### Corresponding Author

\*E-mail: [christa.fittschen@univ-lille1.fr](mailto:christa.fittschen@univ-lille1.fr).

## ACKNOWLEDGMENT

The laboratory participates in the Institut de Recherche en ENvironnement Industriel (IRENI), which is financed by Région Nord Pas-de-Calais, the Ministère de l'Enseignement Supérieur et de la Recherche, the CNRS, and European Regional Development Fund (ERDF). The authors are thankful for financial support through the "Program Hubert Curien" Balaton. C.J. thanks the European Union for financial support through project MEST-CT-2005-020659.

## REFERENCES

- (1) Volkamer, R.; Sheehy, P.; Molina, L. T.; Molina, M. J. *Atmos. Chem. Phys.* **2010**, *10*, 6969–6991.
- (2) Liao, W.; Case, A. T.; Mastromarino, J.; Tan, D.; Dibb, J. E. *Geophys. Res. Lett.* **2006**, *33*, L09810.
- (3) Hellebust, S.; Roddis, T.; Sodeau, J. R. *J. Phys. Chem. A* **2007**, *111*, 1167–1171.
- (4) Monge, M. E.; D'Anna, B.; George, C. *Phys. Chem. Chem. Phys.* **2010**, *12*, 8991–8998.
- (5) Langridge, J. M.; Gustafsson, R. J.; Griffiths, P. T.; Cox, R. A.; Lambert, R. M.; Jones, R. L. *Atmos. Environ.* **2009**, *43*, 5128–5131.
- (6) Rohrer, F.; Bohn, B.; Brauers, T.; Bröning, D.; Johnen, F.-J.; Wahner, A.; Kleffmann, J. *Atmos. Chem. Phys.* **2005**, *5*, 2189–2201.
- (7) Djehiche, M.; Tomas, A.; Fittschen, C.; Coddeville, P. *Environ. Sci. Technol.* **2011**, *45*, 608–614.
- (8) Jain, C.; Parker, A. E.; Schoemaeker, C.; Fittschen, C. *Chem-PhysChem* **2010**, *11*, 3867–3873.
- (9) Aluculesei, A.; Tomas, A.; Schoemaeker, C.; Fittschen, C. *Appl. Phys. B: Lasers Opt.* **2008**, *92*, 379–385.
- (10) Perner, D.; Platt, U. *Geophys. Res. Lett.* **1979**, *6*, 917–920.
- (11) Karlsson, R. S.; Ljungstrom, E. B. *Environ. Sci. Technol.* **1996**, *30*, 2008–2013.
- (12) Yamano, D.; Yabushita, A.; Kawasaki, M.; Perrin, A. *J. Quant. Spectrosc. Radiat. Transfer* **2010**, *111*, 45–51.
- (13) Sironneau, V.; Orphal, J.; Demaison, J.; Chelin, P. *J. Phys. Chem. A* **2008**, *112*, 10697–10702.
- (14) Guilmoit, J. M.; Godefroid, M.; Herman, M. *J. Mol. Spectrosc.* **1993**, *160*, 387–400.
- (15) Guilmoit, J. M.; Melen, F.; Herman, M. *J. Mol. Spectrosc.* **1993**, *160*, 401–410.
- (16) Stockwell, W. R.; Calvert, J. G. *J. Photochem.* **1978**, *8*, 193–203.
- (17) Febo, A.; Perrino, C.; Gherardi, M.; Sparapani, R. *Environ. Sci. Technol.* **1995**, *29*, 2390–2395.
- (18) Stutz, J.; Kim, E. S.; Platt, U.; Bruno, P.; Perrino, C.; Febo, A. *J. Geophys. Res.* **2000**, *105*, 14585–14592.
- (19) Barney, W. S.; Wingen, L. M.; Lakin, M. J.; Brauers, T.; Stutz, J.; Finlayson-Pitts, B. J. *J. Phys. Chem. A* **2000**, *104*, 1692–1699.
- (20) Varma, R.; Curl, R. F. *J. Phys. Chem.* **1976**, *80*, 402–409.
- (21) Thiebaud, J.; Crunaire, S.; Fittschen, C. *J. Phys. Chem. A* **2007**, *111*, 6959–6966.
- (22) Tang, Y.; Tyndall, G. S.; Orlando, J. J. *J. Phys. Chem. A* **2010**, *114*, 369–378.
- (23) Thiebaud, J.; Fittschen, C. *Appl. Phys. B: Lasers Opt.* **2006**, *85*, 383–389.
- (24) Parker, A.; Jain, C.; Schoemaeker, C.; Szriftgiser, P.; Votava, O.; Fittschen, C. *Appl. Phys. B: Lasers Opt.* **2011**, *103*, 725–733.
- (25) Thiebaud, J.; Aluculesei, A.; Fittschen, C. *J. Chem. Phys.* **2007**, *126*, 186101.
- (26) Vaghjiani, G. L.; Ravishankara, A. R. *J. Chem. Phys.* **1990**, *92*, 996–1003.
- (27) Johansson, O.; Bood, J.; Alden, M.; Lindblad, U. *Appl. Phys. B: Lasers Opt.* **2009**, *97*, 515–522.
- (28) Vaghjiani, G.; Ravishankara, A. *J. Geophys. Res.* **1989**, *94*, 3487–3492.
- (29) Forster, R.; Frost, M.; Fulle, D.; Hamann, H. F.; Hippler, H.; Schlepegrell, A.; Troe, J. *J. Chem. Phys.* **1995**, *103*, 2949–2958.

- (30) Butkovskaya, N. I.; Kukui, A.; Pouvesle, N.; Bras, G. L. *J. Phys. Chem. A* **2005**, *109*, 6509–6520.
- (31) Burkholder, J. B.; Mellouki, A.; Talukdar, R.; Ravishankara, A. R. *Int. J. Chem. Kinetics* **1992**, *24*, 711–725.
- (32) Atkinson, R.; Baulch, D. L.; Cox, R. A.; Crowley, J. N.; Hampson, R. F.; Hynes, R. G.; Jenkin, M. E.; Rossi, M. J.; Troe, J. *Atmos. Chem. Phys.* **2004**, *4*, 1461–1738.
- (33) Macko, P.; Romanini, D.; Mikhailenko, S. N.; Naumenko, O. V.; Kassi, S.; Jenouvrier, A.; Tyuterev, G.; Campargue, A. *J. Mol. Spectrosc.* **2004**, *227*, 90–108.
- (34) Wojdyr, M. *J. Appl. Cryst.* **2010**, *43*, 1126–1128.